


FULL PAPER

Open Access



Subsurface velocity structure and site amplification characteristics in Mashiki Town, Kumamoto Prefecture, Japan, inferred from microtremor and aftershock recordings of the 2016 Kumamoto earthquakes

Takumi Hayashida^{1*} , Masumi Yamada², Masayuki Yamada³, Koji Hada³, Jim Mori², Yoshinori Fujino³, Hiromu Sakaue⁴, Sosuke Fukatsu³, Eiko Nishihara³, Toru Ouchi³ and Akio Fujii³

Abstract

In order to investigate the seismic velocity structure in the region of concentrated severe damage during the 2016 Kumamoto earthquake sequence, we conducted continuous seismic observations in the central area of Mashiki Town, Kumamoto Prefecture. During 4 days of observations at eight temporary sites, 2 months after the mainshock, recordings from 30 aftershocks ($1.7 \leq M_i \leq 4.3$, $1.9 \text{ km} \leq \text{depth} \leq 13.5 \text{ km}$) were obtained. The aftershock data showed that site amplifications at approximately 1 Hz are dominant in a zone where almost no buildings were damaged along the Akitsu riverside, whereas site amplifications at higher than 3 Hz are observed in the heavily damaged zones. Our data also showed that the peak acceleration and velocity amplitudes, as well as seismic intensities for the small events in the less damaged zone, are clearly larger than those in the damaged zones, implying that the damage distribution is inconsistent with site response based on linear site amplifications. The estimated phase velocities of Rayleigh waves using the aftershock and microtremor data show dispersive characteristics in the lower frequency range ($0.26 \leq f \leq 1.27 \text{ Hz}$), but the values are substantially smaller than those derived from the P–S logging model at the nearest KiK-net strong-motion observation station KMMH16. The derived microtremor horizontal-to-vertical spectral ratios and earthquake radial-to-vertical (R/V) spectral ratios show common distinct peaks at around 0.4 Hz, which are possibly related to the response of deep sedimentary layers beneath the area. The refined velocity structure model that better accounts for both the phase velocity and common dominant peak indicates that the values of S wave velocity (V_s) above the bedrock layer ($V_s = 2700 \text{ m/s}$) are smaller than those inferred from the logging model and the depth to the bedrock layer could be much deeper (about 600 m) in comparison with the logging model (234 m). The derived R/V spectral ratio at station KMMH16 also shows a distinct peak at 0.4 Hz, suggesting that there is no large difference of deep sedimentary structure between the observation area and station KMMH16.

Keywords: 2016 Kumamoto earthquake, Aftershock, Ground motion, Site amplification, Microtremor, Surface wave, Phase velocity

*Correspondence: takumi-h@kenken.go.jp

¹ International Institute of Seismology and Earthquake Engineering, Building Research Institute, 1 Tachihara, Tsukuba, Ibaraki 305-0802, Japan
Full list of author information is available at the end of the article

Introduction

The 2016 Kumamoto earthquake sequence including the largest foreshock (M_W 6.1 on April 14) and the mainshock (M_W 7.1 on April 16) occurred in the central part of Kumamoto Prefecture, southwestern Japan, and caused severe damage in areas between Kumamoto City and Minamiaso Village near the Futagawa and Hinagu fault zones (see the locations in Fig. 1a). Significant surface ruptures associated with the earthquake sequence appeared in Mashiki Town, which is located at the junction of the two major fault zones (Shirahama et al. 2016; Sugito et al. 2016; Toda et al. 2016) and seismic intensity of 7, the maximum seismic intensity scale of the Japan Metrological Agency (JMA), was measured during both larger events. The results of damage investigations (e.g., National Institute for Land and Infrastructure Management and Building Research Institute 2016; Sugino et al.

2016b; Tomozawa et al. 2017; Yamada 2017; Yamada et al. 2017a, b) showed that heavily damaged buildings were concentrated in a narrow region between Kumamoto Prefectural Route 28 (R28) and the Akitsu River running from east to west in the central part of Mashiki (Fig. 1b).

Field surveys after the mainshock also showed that the cause of the varying damage distribution could be explained by different site conditions of this area. According to the landform classification map for flood control published by the Geospatial Information Authority of Japan, the distribution of damaged buildings corresponds well to the river terrace between R28 and the Akitsu River, whereas almost no buildings collapsed in the floodplain and old river channel along the Akitsu riverside (e.g., Yamada 2017; Yamada et al. 2017a, c). These findings indicate that the building damage pattern is strongly affected by the site conditions associated with local subsurface geology. The results of single-point

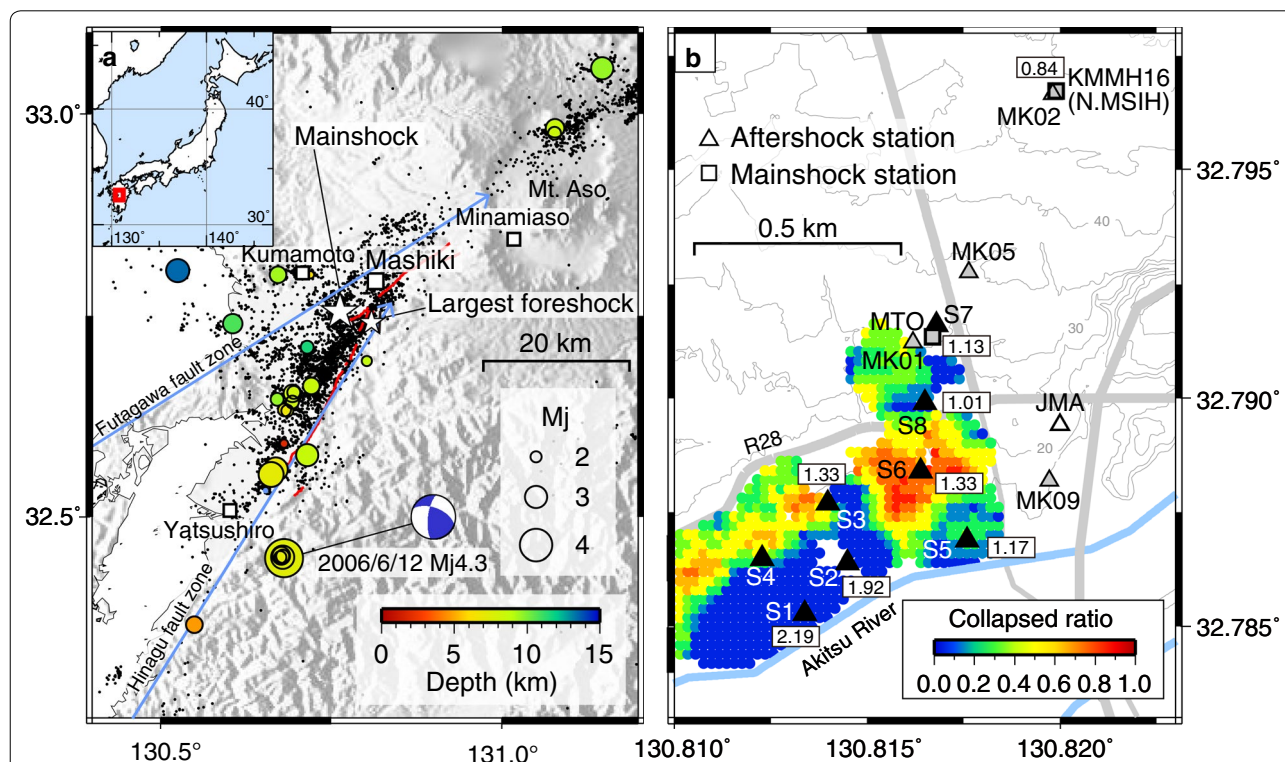


Fig. 1 Maps showing epicenters of recorded aftershocks and locations of temporary aftershock observation sites. **a** Colored circles indicate the locations of 30 aftershocks recorded at the temporary aftershock observation sites. The size of a circle corresponds to the JMA magnitude (M_j) and the color corresponds to the hypocentral depth. Two stars and small black dots indicate epicenters of the largest foreshock (M_j 6.4) and the mainshock (M_j 7.3) of the 2016 Kumamoto earthquake sequence, and the aftershocks that occurred from April 14 through June 9, 2016, respectively. **b** Black triangles show the locations of temporary observation sites deployed in Mashiki (S1–S8). Gray triangles indicate the temporary aftershock observation stations deployed by Yamanaka et al. (2016) in the same area (MK01, MK02, MK05 and MK09) and a white triangle shows the location of seismic intensity meter deployed by JMA. Gray squares show the locations of the seismic intensity observation station inside Mashiki town office (MTO) and the Kik-net strong-motion observation station KMMH16 (same location as the Hi-net station N.MSIH) operated during both the largest foreshock and the mainshock. The calculated JMA seismic intensity values at the temporary sites and station KMMH16 (ground surface) during an event that occurred at 22:08 JST on June 12, 2016 (EQ18: M_j 4.3, depth = 7 km) are also denoted in rectangles. Colored circles indicate the ratio of the totally collapsed wooden buildings identified during a field survey (Yamada et al. 2017a)

microtremor observations in this area (e.g., Kagawa et al. 2017; Kawase et al. 2017; Nagao et al. 2017) showed a clear correlation between the patterns of peak frequency in the horizontal-to-vertical (H/V) spectral ratios and the landform characteristics. Yamada et al. (2017c) performed further microtremor observations with miniature arrays at 108 sites in Mashiki and clarified the differences of Rayleigh wave dispersion characteristics between the damaged and undamaged zones. They found that an extremely low S wave velocity (V_s) layer (< 100 m/s) exists at very shallow depth beneath Mashiki. The estimated thickness of this layer is less than several meters in the severely damaged zones, where the dominant frequencies of microtremor H/V spectral ratio are higher than 2 Hz. In contrast, in the floodplain of the Akitsu River where almost no buildings were collapsed, the low-velocity layer is thicker than 10 m and the dominant H/V frequencies were around 1 Hz.

The predominant frequency of soil layers is fundamental information in seismic microzonation and a reasonable indicator that relates the local site condition to earthquake damage. Past observations of damaging earthquakes in Japan showed that the strong ground motions in the frequency range between 0.5 and 1 Hz greatly affect wooden buildings (e.g., Kitagawa and Hiraiishi 2004; Sakai et al. 2008). The natural frequency of low-rise wooden buildings is between 2 and 10 Hz (e.g., Sugino et al. 2016a), but the frequency may shift to lower values (around 1 Hz) when they are subjected to strong shaking. Therefore, larger damage was expected along the Akitsu river where the frequencies around 1 Hz are dominant. However, the damage investigations showed very different results with relatively light damage close to the river and more severe damage associated with sites of higher natural frequencies that were located farther from the river. Besides the local differences in site conditions, there are several other possible factors that could account for the damage concentration in Mashiki; the construction years of buildings (e.g., Mori et al. 2017; Sugino et al. 2016b; Yamada 2017), types of foundations in the buildings (e.g., Mori et al. 2017), and/or surface fault ruptures (e.g., Suzuki et al. 2016). There were no strong-motion records of the larger events in the heavily damaged zones so that aftershock data recorded in both the damaged and undamaged zones are used to help understand the difference of seismic response.

Recent studies have tried to explain this unusual site amplification in Mashiki using nonlinear site response analyses, assuming that frequencies between 0.5 and 1 Hz were dominant in the heavily damaged zones and lower frequencies were dominant in the less damaged zone. Yamada et al. (2017c) calculated the seismic response for both damaged and undamaged zones of Mashiki using

shallow seismic velocity structure models obtained from microtremor observations with typical nonlinear properties of sand and clay. Shingaki et al. (2017) and Yoshimi et al. (2017) determined dynamic properties of surface soils including volcanic ash clay, using actual soil samples in Mashiki, and Nakagawa et al. (2017) performed time-history response analysis for the mainshock at two sites in Mashiki using the obtained dynamic deformation properties. For analyzing the ground motions of the mainshock, information from the borehole (252 m in depth) of the closest KiK-net strong-motion observation station, KMMH16 (see the location in Fig. 1b) was used. The station is operated by the National Research Institute for Earth Science and Disaster Resilience (NIED) and located about 1 km to the northeast of the severely damaged area. Velocity models obtained from the borehole logging are well constrained for the shallower depths (less than a few tens of meters) but have lower resolution for the deeper structure. Therefore, it is important to evaluate the deep sedimentary structure in the damaged area.

To investigate the differences of ground motion characteristics in the heavily and less damaged zones as well as station KMMH16, we conducted aftershock and microtremor (ambient noise) observations in and around the damaged zones of Mashiki (see the observation locations in Fig. 1b). Figure 1b also shows the locations of aftershock observation stations deployed by Yamanaka et al. (2016) (gray triangles: MK01, MK02, MK05 and MK09) and a seismic intensity station deployed by JMA (white triangle) just after the mainshock. Our aftershock observation sites were installed in the heavily damaged zones, while the existing temporary aftershock stations were located outside of this zone. In this paper, we show the differences of the ground motion characteristics between the contrasting zones and propose a velocity structure model of the entire area for seismic response analysis.

Field observations

The aftershock and microtremor observations were conducted from June 10 to June 13, 2016, 2 months after the mainshock. Dimensions of the observation area are approximately 500 m in the east–west direction and 750 m in the north–south direction, which corresponds to the area of our damage and microtremor surveys (Yamada et al. 2017a, c). This area is a fluvial terrace of the Akitsu River and the altitude increases as a function of distance toward the north from the river. We installed eight accelerometers in and around the damaged zones at intervals of approximately 150–200 m (S1–S8: see Table 1 and Fig. 1b); six sensors between R28 and the Akitsu River and two sensors near the former main building of the Mashiki town office (MTO). A seismic intensity meter managed by the local government was installed at

Table 1 Temporary stations for aftershock observation of the 2016 Kumamoto earthquake

Site	Latitude (°)	Longitude (°)	Altitude ^a (m)	Start	End
S1	32.78533	130.81335	11	2016/06/10 15:51	2016/06/13 13:01
S2	32.78636	130.81449	11	2016/06/10 15:13	2016/06/13 13:34
S3	32.78774	130.81398	14	2016/06/10 14:23	2016/06/13 13:17
S4 ^b	32.78655	130.81231	12	2016/06/10 17:30	2016/06/13 13:50
S5	32.78692	130.81761	12	2016/06/10 17:30	2016/06/13 13:01
S6	32.78837	130.81638	19	2016/06/10 16:30	2016/06/13 13:15
S7	32.79157	130.81685	33	2016/06/10 14:25	2016/06/13 13:44
S8	32.78989	130.81651	21	2016/06/10 15:25	2016/06/13 13:31

^a From the Denshi-kokudo web system (<https://maps.gsi.go.jp/>) provided by the Geospatial Information Authority of Japan

^b Observed data at site S4 were not used in this study

MTO. We used JEP-6A3 (Mitsutoyo Corp.) over-damped accelerometers at sites S1–S4, and SMAR-6A3P (Mitsutoyo Corp.) over-damped accelerometers at the other sites. Each sensor was connected to a 24-bit data logger DATAMARK LS-8800 (Hakusan Corp.), with a sampling frequency at 200 Hz. All the sensors were installed on the ground surface, outside of buildings and power was supplied from external batteries. Both types of sensors have the same response characteristics, except different sensitivities (0.112 V/m/s² for JEP-6A3 and 0.224 V/m/s² for SMAR-6A3P). The pretests confirmed that all of the sensors have the correct frequency response to an input signal between 0.2 and 10.0 Hz for both horizontal and vertical components.

We distributed the sensors in areas with different building damage ratios; sites S1 and S2 were located in a zone with no collapsed buildings near the Akitsu riverside, and the other sites were located in the damaged zones. Figure 1b also shows the ratio of the totally collapsed wooden buildings that correspond to damage grade D5 (story failure) in the damage scale proposed by Okada and Takai (1999). The sensor at site S6 was deployed at a location where 77% of the wooden buildings were collapsed. The distance between site S7 and the station MTO was about 30 m so that we will discuss the ground motion differences between the mainshock observation station and the other temporary stations in the latter part. We excluded the data at site S4 in the following analyses due to a possible problem in the sensor cable, although signals related to earthquake ground motions were recorded.

We also used data from the surface and borehole components of KiK-net station KMMH16 and co-located Hinet station M.MSIH. We confirmed that the frequency responses from 0.14 to 20 Hz were very consistent for the two instruments in the borehole (see an example in Additional file 1: Fig. S1).

Results

Aftershock data on July 12, 2016

Earthquake ground motion data from the aftershocks were manually extracted from the continuously recorded waveforms, based on the unified earthquake catalogue provided by JMA. We selected events with maximum JMA seismic intensity in the Kumamoto Prefecture higher than or equal to 1. Ground motion data from 30 events with clear P- and S wave signals were obtained (see the event information in Table 2 and the hypocenter distribution in Fig. 1a). Epicenters of the aftershocks are in the regions correspond to the middle and northern sections of the Hinagu fault zone, the west part of the Futagawa fault zone and the north side of Mt. Aso. The JMA magnitude (M_j) of the selected events ranged from 1.7 to 4.3 and the depths were relatively shallow (between 1.9 and 13.5 km).

The largest event with M_j 4.3 (M_w 4.2; EQ18 in Table 2) occurred in the southern Yatsushiro City (see the hypocentral location in Fig. 1a) at 22:08 JST on June 12. JMA seismic intensity 5-lower was measured nearby Sakamoto, Yatsushiro City. This event was one of the three events from April 20, 2016, to the present time (June 2018) with maximum JMA seismic intensity larger or equal to 5-lower in Kumamoto Prefecture. Epicentral distance from Mashiki is about 40 km, and JMA seismic intensity of the event was 1 at MTO. Figures 2 and 3 show the observed accelerograms and Fourier amplitude spectra of the M_j 4.3 recordings at the observation sites S1–S8 except S4, together with those for the surface and borehole components of KiK-net station KMMH16. In Fig. 2, the accelerograms recorded at sites S1 and S2 clearly show the long period components and long duration with large amplitude in the horizontal components. The Fourier amplitude spectra at sites S1 and S2 have dominant peaks around 1 Hz in the horizontal components which are not seen at other sites (Fig. 3).

Table 2 List of the detected events

Event	Origin time (JST)	Latitude (°)	Longitude (°)	Depth (km)	M_j
EQ01	2016/06/10 15:41:59.7	32.577	130.715	8.6	3.0
EQ02	2016/06/10 15:44:43.6	32.555	130.669	7.3	2.5
EQ03	2016/06/10 21:21:48.7	32.711	130.715	11.6	2.2
EQ04	2016/06/10 21:32:29.6	32.976	131.077	8.4	2.2
EQ05	2016/06/10 23:38:48.1	32.557	130.649	2.2	1.7
EQ06	2016/06/11 04:58:27.3	32.740	130.606	10.8	2.8
EQ07	2016/06/11 09:56:08.1	32.806	130.525	13.5	3.1
EQ08	2016/06/11 11:59:34.9	32.553	130.662	7.2	3.3
EQ09	2016/06/11 17:08:34.3	32.801	130.720	6.1	1.7
EQ10	2016/06/11 23:41:27.8	32.559	130.669	6.9	3.2
EQ11	2016/06/12 01:17:49.2	33.056	131.147	9.6	3.0
EQ12	2016/06/12 03:56:54.0	32.694	130.802	8.7	1.9
EQ13	2016/06/12 04:35:16.8	32.982	131.078	8.4	2.7
EQ14	2016/06/12 15:58:43.0	32.643	130.693	8.4	2.2
EQ15	2016/06/12 19:47:45.3	32.591	130.681	1.9	1.8
EQ16	2016/06/12 20:31:21.7	32.655	130.695	8.6	2.2
EQ17	2016/06/12 21:20:13.9	32.801	130.672	9.4	2.5
EQ18	2016/06/12 22:08:15.0	32.449	130.681	7.4	4.3
EQ19	2016/06/12 22:53:29.3	32.450	130.679	7.4	3.1
EQ20	2016/06/12 23:08:30.6	32.654	130.693	8.2	2.6
EQ21	2016/06/12 23:12:55.2	32.737	130.628	8.7	2.8
EQ22	2016/06/13 00:00:41.2	32.451	130.679	7.5	2.2
EQ23	2016/06/13 00:39:04.2	32.663	130.721	8.5	2.5
EQ24	2016/06/13 04:03:29.0	32.646	130.671	9.6	2.2
EQ25	2016/06/13 04:21:35.0	32.632	130.686	6.8	2.1
EQ26	2016/06/13 04:46:28.0	32.633	130.682	6.8	2.2
EQ27	2016/06/13 09:26:28.0	32.450	130.676	7.0	2.1
EQ28	2016/06/13 09:39:09.9	32.803	130.705	6.3	1.8
EQ29	2016/06/13 12:34:22.5	32.452	130.677	7.2	2.6
EQ30	2016/06/13 13:13:42.3	32.366	130.550	4.7	2.5

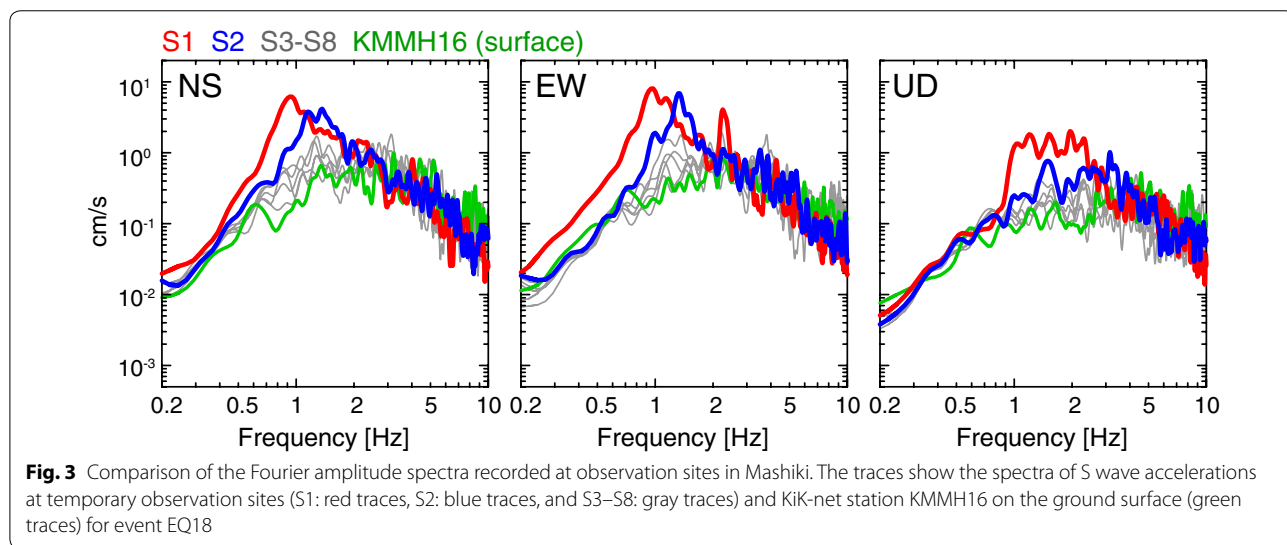
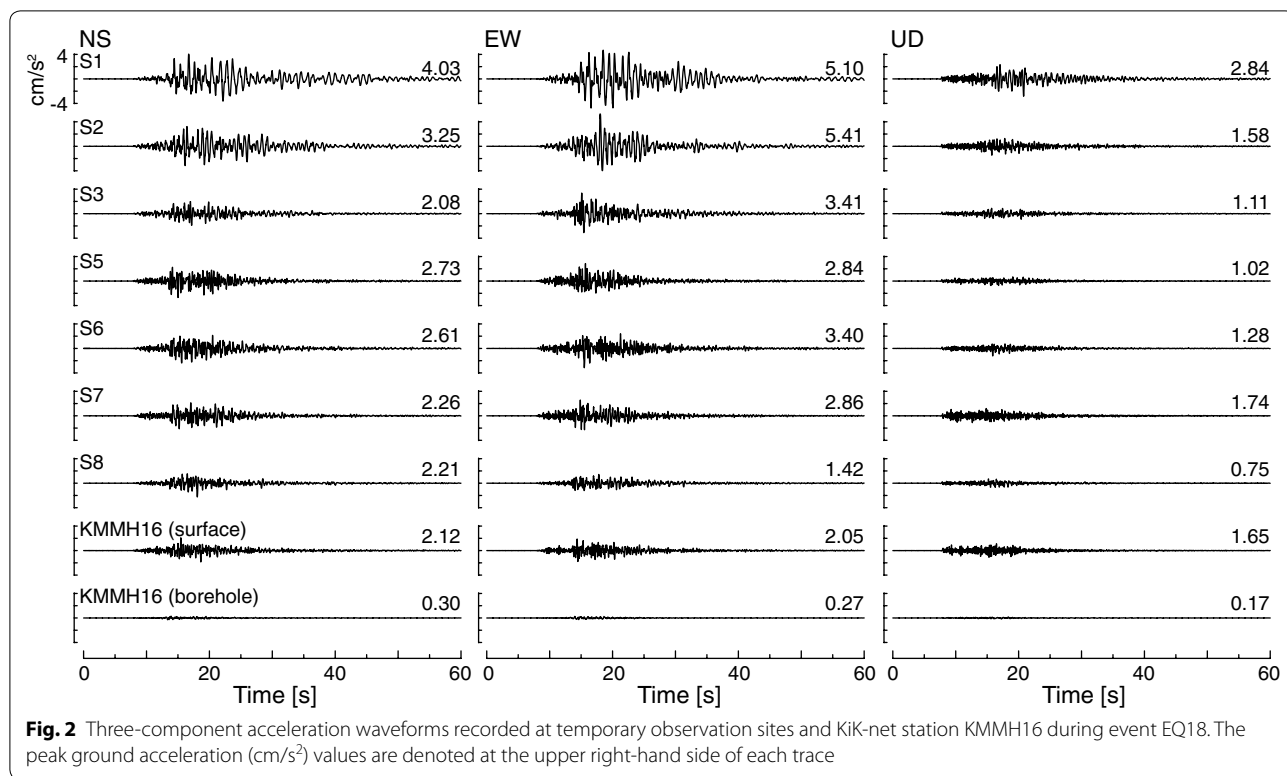
From the unified earthquake catalog provided by JMA

Characteristics of the site amplifications

Figure 4 shows the spectral ratios of the S wave (20.48 s segment from the S wave onsets) between our surface observation sites and the borehole station M.MSIH, for all the detected events. A cosine taper was applied to both sides of the S wave segments with a 5% width of the segment time length. Assuming that the input ground motions beneath our observation area and KMMH16 station are similar and the S wave is dominant in the segments, the spectral ratios represent the approximate borehole to surface S wave transfer functions of subsurface layers at each site. The shapes of the derived spectral ratios look slightly different between the NS and EW components at some sites possibly due to the complex velocity structure, but there are no significant differences in the dominant peak frequencies. The spectral ratios clearly show dominant peaks around 1–2 Hz at sites

S1 and S2 with amplitudes greater than 20, while other sites show peaks at higher frequencies (> 3 Hz). This is consistent with the results of past microtremor surveys which showed site amplifications at around 1 Hz near the Akitsu River (Kawase et al. 2017; Nagao et al. 2017; Yamada et al. 2017c).

Next, we obtained H/V spectral ratios at each observation site from the ambient noise sections of the recordings. The derived probability density functions for our continuous data show the measurable frequency range of microtremor down to 0.2 Hz (see an example in Additional file 1: Fig. S2). We selected 1-h continuous waveform data during a quiet period of the 4-day continuous records (between 0:00 and 1:00 JST on June 11). The three-component recordings were divided into 40.96 s window segments with 50% overlap, and fast Fourier transforms were applied to each segment. Then,



the H/V ratios were computed and smoothed using a Parzen window with bandwidth of 0.1 Hz, and all the ratios were stacked together. Note that we removed segments with large amplitude irregular noise in advance and the total number of segments used for the analysis was more than 140 for each site. Figure 5 shows the derived microtremor H/V ratios, as well as the spectral

ratios of the north–south and east–west horizontal components with the vertical component (NS/V and EW/V, respectively) at all observation sites. The derived spectral ratios indicate predominant peaks in the frequency around 1–2 Hz at sites S1 and S2, where there was no building damage. This feature is consistent with the surface/borehole spectral ratios derived from our aftershock data. The trend in the dominant frequency

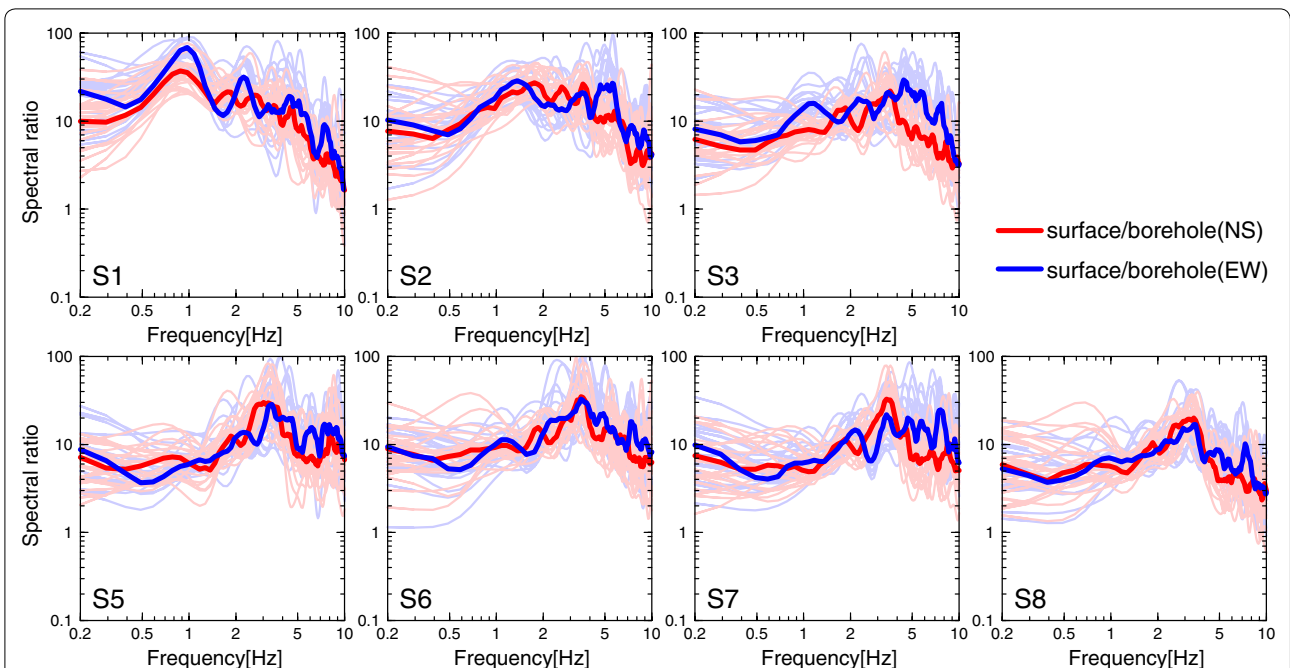


Fig. 4 Fourier spectral ratios between each temporary aftershock observation site and Hi-net station N.MSIH for all detected events. Blue and red traces show the ratios for the S wave portions from NS and EW components, respectively. Thin traces show the spectral ratios derived for each event and thick traces corresponds to the median values. Note that the sampling frequencies at the temporary sites have been reduced to 100 Hz

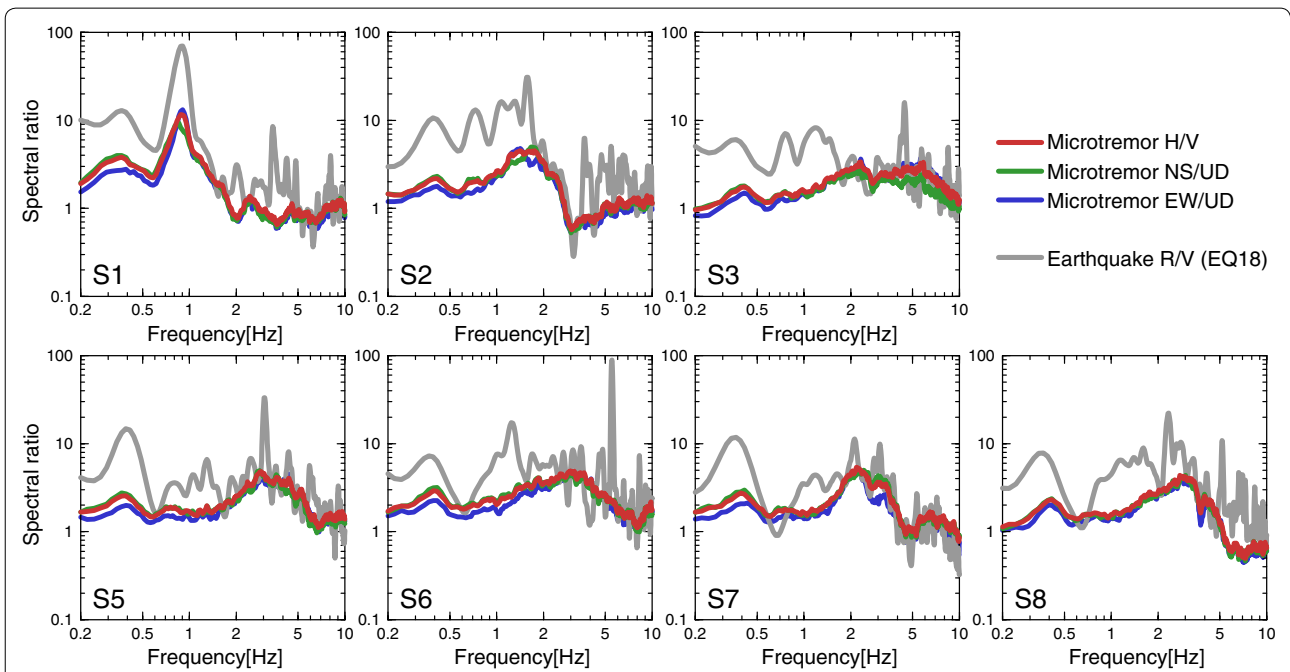


Fig. 5 Microtremor spectral ratios derived at each observation site. Green, red and blue traces show H/V, NS/V and EW/V spectral ratios, respectively. Gray traces show the radial-to-vertical (R/V) spectral ratios of S-coda waves for event EQ18

is also comparable with the results of single-station microtremor H/V spectral ratios (Yamada et al. 2017c).

We also derived earthquake radial-to-vertical (R/V) spectral ratios using the data of event EQ18 (M_j 4.3 and M_w 4.2) that contain surface waves in the coda. After rotation of the two horizontal components (NS and EW) to radial and transverse components with respect to each source-sensor azimuth, we selected 20.48 s segments from 10 s after the S wave arrivals. The spectral ratios of radial-to-vertical motions that would correspond to Rayleigh wave ellipticity were computed at each site. Here, the same smoothing filter as the microtremor H/V calculations above was applied. Figure 5 also shows the derived earthquake R/V ratios at each observation site. They show peak frequencies similar to the H/V spectra and the predominant peaks (ratios of 30 or greater) around 1–2 Hz are also seen at sites S1 and S2. The peaks at 1–2 Hz are also recognized at sites S3, S5, S6 and S8, but the ratios are substantially smaller (between 5 and 20) compared to those in the less damaged zone and other predominant peaks with larger values are seen at the higher frequency range (> 2 Hz).

Besides the predominant peaks at frequencies higher than 1 Hz, there are distinct peaks at 0.4 Hz for all the spectra, especially at S5–S8. This peak can also be observed in the microtremor H/V spectra with smaller amplitudes. The common dominant peaks of the microtremor H/V and earthquake R/V ratios at this lower frequency are possibly related to the response of deep sedimentary layers beneath the area, which will be discussed in a later section.

Rayleigh wave phase velocity

We estimated dispersion characteristics of Rayleigh wave phase velocities in the lower frequency range using continuous microtremor and event data. We applied the two-site SPAC (2sSPAC) method (e.g., Morikawa et al. 2004; Hayashi et al. 2013) for the microtremor data, assuming that the microtremor wave-field around the area is spatially and temporally uniform. We selected four sensor pairs around the heavily damaged zones (S6–S8: 167 m, S5–S8: 201 m, S3–S6: 238 m, and S3–S5: 349 m) for the data processing. We used the vertical component of microtremors recorded during the entire observation period (from June 10, 18:00 to June 13, 13:00). At first, 1-h continuous data were divided into 87 segments (time window of 40.96 s) without overlap. After removal of segments containing irregular noise or earthquake signals, fast Fourier transforms were performed on the datasets and the complex coherence functions between the selected site-to-site pairs were calculated. The coherence functions from all the segments were stacked and an hourly stacked coherence function was derived. If an

hourly derived coherence function showed small values around 1 Hz in comparison with many other traces, indicating small coherence between the two datasets, those data were excluded. Finally, all the hourly derived coherence functions were summed and the averaged function (with the variance) was regarded as the SPAC coefficients for the sensor pair. The Rayleigh wave phase velocities were estimated from the derived SPAC coefficients using a fifth-degree polynomial that approximates the inverse function of the zero order Bessel function of the first kind. The frequency range we used for the determination of phase velocity depended on the sensor distance; it is determined so that the wavelength corresponding to the estimated phase velocity was 2–7 times the sensor distances. The estimated phase velocity dispersion curves from the four sensor-to-sensor pairs were combined to derive a single dispersion curve. Since each SPAC coefficient curve has the variance so that the dispersion curve has been derived by the inverse-variance weighted method. The coherence functions of microtremors are not always stable in the lower frequency band due to the low detection performances and the final accepted frequency range for the 2sSPAC analysis was between 0.98 and 1.27 Hz (Fig. 6a).

We also estimated the Rayleigh wave phase velocities from aftershock data (event EQ18) based on the semblance analysis of the S-coda wave (Fukumoto et al. 2004), assuming that the coda wave is dominated by surface waves. The phase velocities were estimated at frequencies from 0.2 to 0.9 Hz with an interval of 0.01 Hz, using narrow-band velocity waveforms (0.9 and 1.1 times the target frequency for the low-frequency and the high-frequency cutoffs, respectively) in the vertical component. The length of the time window for the analysis is twice the reciprocal of the target frequency, and the window was shifted every 0.5 s throughout the dominant wave train. For each time window, the apparent velocity as well as incident angle was calculated. The derived apparent velocities with sufficient semblance values (≥ 0.9) were averaged, and the phase velocity for each frequency was determined.

Figure 6a shows the estimated dispersion curve for the Rayleigh wave phase velocity using both microtremor and event data. The error bars indicate that the standard deviations are low for the entire frequency range, except around 0.7 Hz. The estimated dispersion curves of Rayleigh wave phase velocity from the miniature microtremor arrays (Yamada et al. 2017c) at around sites S1 (array A059), S6 (array A026), S7 (array A001) and station KMMH16 (array A000) are also shown in the figure. The estimated phase velocities vary with the sites but are less than 1000 m/s at the target frequencies of the miniature microtremor surveys (> 1.7 Hz), which is consistent with

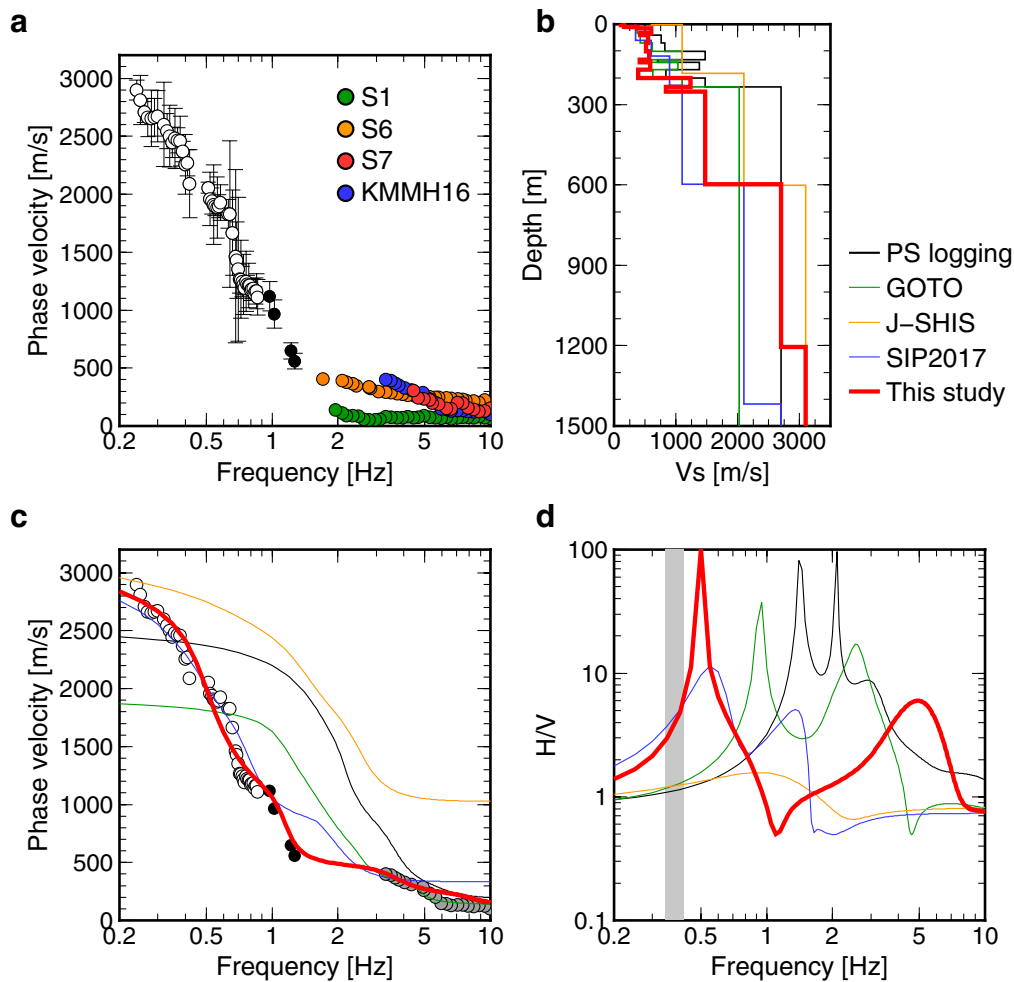


Fig. 6 Comparisons of estimated phase velocity dispersion curves, subsurface structure models and the corresponding theoretical H/V ratios. **a** Circles show the estimated phase velocities of Rayleigh waves using event data (white) and microtremor data (black), as well as miniature microtremor array data (Yamada et al. 2017c) for nearby station KMMH16 (blue) and the aftershock observation sites (S1: green, S6: orange, and S7: red). **b** Vs structure models used in this study. The P–S logging model at the nearest KiK-net strong-motion observation station KMMH16, GOTO model (Goto et al. 2016), J-SHIS model, SIP2017 model (Ogawa et al. 2017; Senna et al. 2017a, b) and our estimated model are shown in black, green, orange, blue and red traces, respectively. **c** Theoretical dispersion curves of the Rayleigh wave phase velocities calculated with models in (b). **d** Theoretical H/V ratios calculated for models in (b). Gray shaded area indicates the frequency range in which the dominant peaks of microtremor H/V ratios are detected

our phase velocity results. For the semblance analysis, we obtained dispersive characteristics of phase velocities in the frequency range between 0.24 and 0.86 Hz. The estimated phase velocities from microtremor and event data also show similar continuous characteristics for the common frequency range, suggesting that our estimations are reasonable.

S wave velocity structure model beneath KiK-net station KMMH16

We refined the P–S logging model at the closest KiK-net station KMMH16 (see Table 3 and Fig. 6b) by using our

dispersion curve of Rayleigh wave phase velocity. We performed velocity structure inversions using a genetic algorithm (GA) technique (Yamanaka and Ishida 1996) to obtain a velocity structure model that can explain the estimated Rayleigh wave dispersion curve.

There are several previous velocity structure models in this area. The P–S logging model at KiK-net station KMMH16 has information down to 252 m depth. Goto et al. (2016) tuned the KiK-net logging model (hereinafter called GOTO model; see Table 3) using the surface/borehole spectral ratio of the small event data. They inverted for Vs values of the top five layers to fit the

Table 3 Seismic velocity structures at KiK-net Mashiki station (KMMH16)

Layer no.	Thickness (m)	Depth (m)	V_p (m/s)	Density (kg/m ³)	V_s (m/s)		
					PS logging	GOTO	This study
1	3	3	240	1220	110	110	110
2	6	9	380	1370	240	160	160
3	6	15	380	1370	240	370	370
4	18	33	1180	1820	500	600	600
5	8	41	1180	1820	400	425	425
6	28	69	1950	2060	760	570	551
7	32	101	2300	2150	820	615	517
8	32	133	2800	2260	1470	1103	564
9	10	143	2800	2260	700	525	415
10	26	169	2800	2260	1380	1035	587
11	32	201	2300	2150	840	630	392
12	33	234	2300	2150	1470	1103	1239
13	18 ^a	252 ^a	2300	2150	–	–	841
14	345 ^a	597 ^a	2300	2150	–	–	1470
15	608 ^a	1205 ^a	4800	2580	2700	2025	2700
16	1411 ^a	2616 ^a	5360	2650	–	–	3100
17	5000 ^a	7616 ^a	5700	2690	–	–	3300
18	–	–	6000	2730	–	–	3400

^a Parameters only for the optimized velocity model in this study

surface/borehole spectral ratio, and used 75% of the V_s in the logging model for the 6th–12th layers due to the limited sensitivity to the deeper structure (Table 3). For deeper structures, the Seismic Hazard Information Station of NIED (J-SHIS: <http://www.j-shis.bosai.go.jp>) provides a nationwide velocity model based on the borehole logging, reflection and gravity surveys. In the J-SHIS model, the velocity structure beneath the target area consists of six layers; three subsurface layers ($600 \text{ m/s} \leq V_s \leq 2100 \text{ m/s}$) along with three upper crustal layers ($3100 \text{ m/s} \leq V_s \leq 3400 \text{ m/s}$). Figure 6c shows the theoretical dispersion curves obtained from the KiK-net logging data, GOTO and J-SHIS models, respectively. The KiK-net P–S logging model clearly overestimates the Rayleigh wave velocity for almost the entire frequency range, suggesting the actual V_s values are much lower than those of the logging model. The GOTO model explains the dispersion curve reasonably well at the higher frequency range (3–10 Hz) that corresponds to the target frequency range of miniature microtremor survey at the site (Yamada et al. 2017c), but still underestimates the lower frequency range even after the 75% reduction of V_s . The observed dispersion curve in Fig. 6c suggests that the hard rock layer ($V_s > 3000 \text{ m/s}$) as in the J-SHIS model is necessary to explain the low-frequency range of the dispersion curve.

We constructed an initial model for the GA in the following procedure. We directly use the GOTO model for

the top five layers, since the theoretical dispersion curve explains the observed dispersion curve at the higher frequency range. We also use the GOTO model as the starting model for the 6th–12th layers in the inversion. Due to the uncertainty of the deeper structure, we use the thicknesses and V_s values of the J-SHIS model for the layers of bedrock ($V_s \geq 2700 \text{ m/s}$). In the preliminary analysis, we found that the $V_s = 2700 \text{ m/s}$ layer in the P–S logging model (234 m) is too shallow to explain our dispersion curve. Therefore, we assumed that the layer would be deeper than the depth of the borehole. Based on this assumption, we modified the properties of the 13th layer in the GOTO model to those of the 12th layer, and added an extra layer ($V_s = 1470 \text{ m/s}$) underneath the borehole with an unknown depth.

In total, we have 18 layers for our initial velocity model: the 1st–5th layers of the GOTO model, 6th–13th layers of the GOTO model for which V_s values will be determined, 14th layer with $V_s = 1470 \text{ m/s}$ with unknown thickness, and four bedrock layers of the J-SHIS model with $V_s = 2700$ – 3400 m/s at the bottom (Table 3). Since there is a trade-off between V_s and thickness of layers, we fix the thickness for the 1st–13th layers and the V_s for the 14th layers just above the bedrock. Other observations such as receiver functions might reduce trade-offs between the velocity and thickness of each layer; however, the small events (M3 and smaller) in our dataset were not appropriate for this method. Therefore, we validate

the reliability of the inversion results focusing on the predominant frequency of the theoretical microtremor H/V, as well as the travel-times of body waves between the ground surface and borehole sensor depth in comparison with the GOTO model. The determined parameters for the inversion are Vs values of eight layers and thickness of the 14th layer; the range of the parameter search for Vs is $\pm 50\%$ of the initial value, and 0–1024 m for the thickness. Since there is no available information on the density profile at station KMMH16, we assigned the parameters based on the relation between Vp and density (Gardner et al. 1974). In the GA optimization, the number of generations that corresponds to the total number of iteration is 500 and the number of population in each generation is 30. Crossover and mutation rates were set to 0.5 and 0.01, respectively. We repeated this optimization process twice by setting the output of the first process as an input of the second process, so that the most optimal values are inside of the range of the parameter search. We used a subroutine program package DISPER80 (Saito 1988) to compute the theoretical dispersion curves for the generated models.

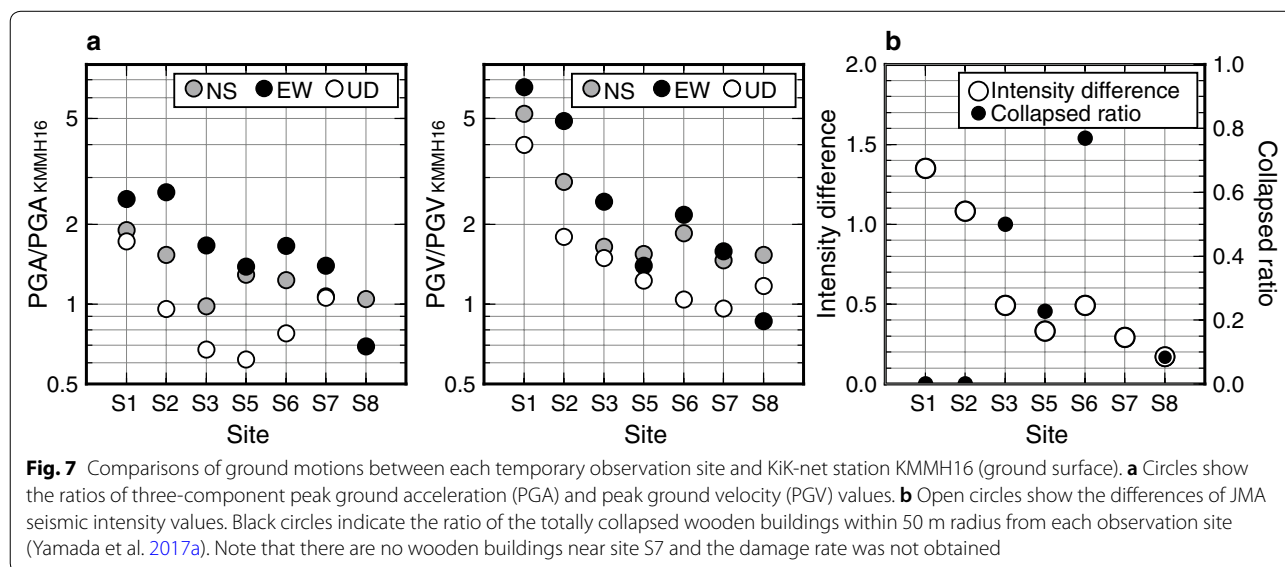
The optimal velocity profile is shown in Fig. 6b and Table 3 with the phase velocities of Rayleigh wave, and theoretical H/V ratios are shown in Fig. 6c, d, respectively. The estimated values for Vs at the 6th–13th layers are substantially smaller than those of the logging model and GOTO model. The estimated depth of the bedrock layer is about 600 m. The comparisons of H/V ratios and phase velocities show that the agreements between the theoretical and estimated phase velocities are substantially improved. Also, the H/V spectral peak around 0.4 Hz is reproduced well by our model, which does not

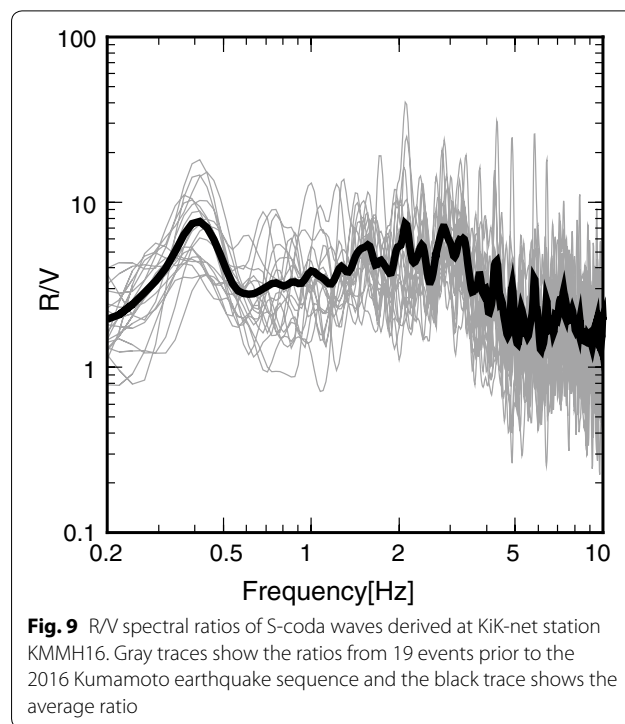
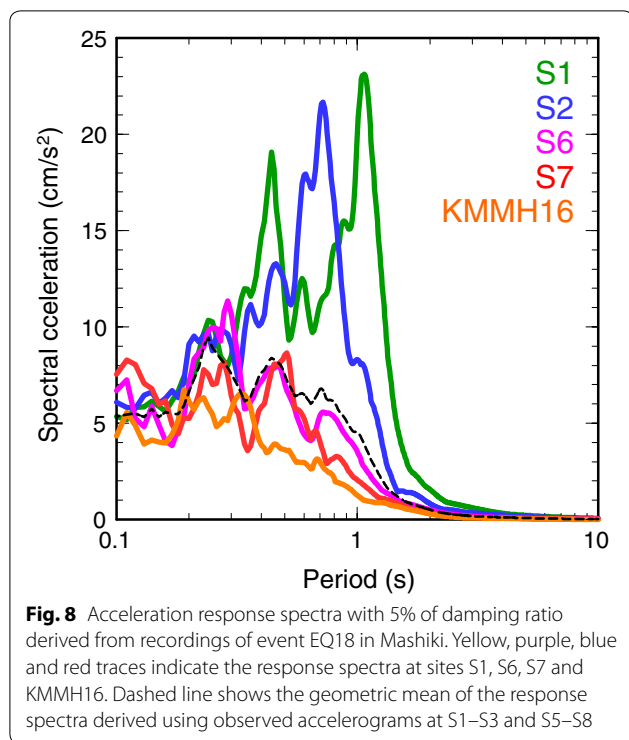
appear in the theoretical H/V spectra of the P–S logging model and GOTO model. Based on the quarter wavelength law, this peak reflects the velocity contrast of the bedrock, suggesting that the bedrock depth can be much deeper than the logging data (234 m).

Discussion

Earthquake damage and site amplification

We discuss the relationship between the damage distribution and the largest aftershock (EQ18) during our observation period. For various ground motion measures, Fig. 7a, b shows the ratios of the peak ground acceleration (PGA) and peak ground velocity (PGV), and the differences of the JMA seismic intensity values between our observation sites and the KiK-net KMMH16 surface station (actual seismic intensity values are shown in Fig. 1b), respectively. Figure 7b also shows the ratios of the totally collapsed wooden buildings within 50 m radius at each site. Note that site S7 was located inside the town office where there were no houses nearby and the damage ratio was not available. This also shows that the ground motions of EQ18 are larger than those at other sites at sites S1 and S2 where there were no collapsed buildings around the sensors sites during the largest foreshock and mainshock. Figure 8 shows the acceleration response spectra for the EW component using the data of EQ18 at sites S1, S2, S6, S7 and KMMH16 together with the geometrical mean of the spectra (sites S1–S3, S5–S8). This clearly indicates that the different site response between the minimally damaged zone (S1 and S2) and the severely damaged zones (S6) as well as site nearby MTO (S7) and station KMMH16, and that the larger response at around 1 Hz can be seen only in the less damaged zone.





As we expected from microtremor geotechnical surveys, our aftershock data show that ground motions around 1 Hz were amplified on the floodplain of the Akitsu River, while the amplification of this frequency range is much less in the damaged zone. This observation is inconsistent with the damage distribution of the mainshock, which shows severe damage away from the river. We need to consider other mechanisms, such as nonlinear site amplification, to explain the strong ground motions in Mashiki.

Comparisons of the velocity model with existing models

We determined a subsurface V_s structure model above the seismic bedrock with the derived dispersion curves of Rayleigh-wave phase velocities from our 4-day observation data in the entire area and miniature microtremor array at KiK-net station KMMH16. We assumed that the deep sedimentary layers for the damaged area are the same as in the vicinity of station KMMH16. If the assumption is correct, the dominant peak around 0.4 Hz in the earthquake R/V spectral ratios that corresponds to the velocity contrast at the seismic bedrock, should be seen in the KMMH16 data. Figure 9 shows R/V spectral ratios at station KMMH16 computed from the 19 shallow crustal earthquakes ($>M4$) that occurred prior to the 2016 Kumamoto earthquake (see the earthquake lists in Table 4). The length of the time window and the bandwidth for smoothing is the same as the R/V analysis. This

averaged spectrum also shows the peak at 0.4 Hz, which suggests that the velocity contrast should exist over a relatively wide area, at least across the area of our aftershock observations and the KiK-net KMMH16 station.

We would like to compare our velocity model to other existing models. In the nationwide J-SHIS model, the depth of the bottom of the subsurface layers is 602 m, which is consistent with our estimation. Since the shallower part of the structure with low V_s (<600 m/s) is not included in the J-SHIS model, the shallow velocity was greatly overestimated and the computed dispersion curve of Rayleigh waves beneath Mashiki has a large discrepancy with our observed dispersion curve (Fig. 6c). Also, the peak in the H/V spectrum at 0.4 Hz could not be explained (Fig. 6d). A group in NIED conducted microtremor observations with large-sized arrays after the Kumamoto earthquake and constructed a three-dimensional (3D) structure model of the deep sedimentary layers (Ogawa et al. 2017; Senna et al. 2017a, b). In their model (hereinafter called SIP2017 model), the velocity structure consists of five subsurface layers ($350 \text{ m/s} \leq V_s \leq 2100 \text{ m/s}$) and the bedrock layer ($V_s = 2700 \text{ m/s}$) that was not included in the J-SHIS model. The velocity profile, theoretical H/V ratio, and dispersion curve of Rayleigh wave phase velocity computed from the SIP2017 model are shown in Fig. 6b–d, respectively. The depth to the bedrock layer in the SIP2017 model is much deeper than the P–S logging

Table 4 Events used for calculation of earthquake R/V ratios at station KMMH16

Origin time (JST)	Latitude (°)	Longitude (°)	Depth (km)	M_j
2003/11/30 12:45:36.3	31.974	130.331	10.1	4.8
2004/04/21 12:20:53.1	31.564	131.838	25.0	5.0
2004/11/21 09:27:42.0	32.502	130.555	9.7	4.1
2004/12/12 14:28:43.4	31.767	129.181	14.7	5.1
2005/03/20 10:53:40.3	33.739	130.176	9.2	7.0
2005/03/21 23:59:21.9	33.785	130.101	12.0	4.8
2005/03/22 15:55:33.5	33.725	130.177	10.5	5.4
2005/03/25 21:03:19.8	33.786	130.118	12.1	4.1
2005/06/03 04:16:41.8	32.495	130.548	10.9	4.8
2006/02/04 00:11:55.6	32.083	129.880	11.6	5.1
2007/03/22 18:27:30.4	32.619	130.828	5.5	4.0
2007/03/23 22:37:05.8	32.619	130.827	6.0	4.1
2007/09/24 17:12:36.0	32.577	129.970	13.8	4.1
2009/06/25 23:03:56.8	33.369	130.893	11.5	4.7
2011/10/05 23:33:27.6	32.914	130.850	9.7	4.5
2012/06/04 15:51:00.0	32.061	130.924	8.8	4.4
2013/03/11 18:34:49.6	31.575	131.858	24.5	5.2
2015/05/27 16:11:07.7	33.031	130.485	8.1	4.0
2015/11/14 05:51:30.1	30.943	128.590	17.0	7.1

From the unified earthquake catalog provided by JMA

model and the consistency between the estimated and theoretical phase velocity characteristics are reasonable in comparison with the J-SHIS model, although the peak frequency of the theoretical H/V is slightly higher than that of our observations. Our velocity model calibrated by the existing V_s profile at the KiK-net KMMH16 site (Goto et al. 2016) and dispersion curve of Rayleigh wave phase velocity can explain the H/V peak reasonably well. In the SIP2017 model the depth to the $V_s=2700$ m/s layer (1417 m) is much deeper than our estimation but the depth of the high- V_s layer ($V_s=2100$ m/s) above the bedrock layer (597 m), which was not included in our model, is very close to our estimated bedrock depth, indicating that the difference in starting structure models for inversions produced different solutions for the bedrock depth. The exact depth of the bedrock for this area is still controversial, but at least both observations suggest that the depth of $V_s>2000$ m/s layer is much deeper than that of the KiK-net logging data (234 m) and is expected to be about 600 m. Our aftershock data and velocity model help improve knowledge of the deep sedimentary structure model in this area.

Conclusions

We conducted aftershock and microtremor observations at eight sites in and around the damaged areas in Mashiki Town, Kumamoto Prefecture, 2 months after the 2016

Kumamoto earthquakes. The aftershock data indicate that site amplifications at approximately 1 Hz are significant during the small events in the less damaged zone where a thick low-velocity surface layer exists, whereas the dominant frequencies are higher than 3 Hz in the damaged zones. These trends are similar to the results from microtremor surveys in the area, indicating that the characteristics of ground motions for the mainshock and small earthquakes show opposite trends in Mashiki. Our observations support the idea that the dominant frequencies of the heavily damaged area were shifted to 1–2 Hz which has a great effect on wooden buildings during the largest foreshock and mainshock, while in the less damaged zone, the 1–2 Hz peaks would be shifted to much lower frequency range, which had less effect on the buildings. The estimated phase velocities of Rayleigh wave using microtremor data as well as the aftershock data (EQ18) are smaller than those of the P–S logging model at the KiK-net station KMMH16. The derived microtremor H/V and earthquake R/V ratios from our data show common dominant peaks around 0.4 Hz, which is possibly related to the response of deeper structure beneath the observation area. We performed a GA inversion for the deep sedimentary structure model with the derived phase velocities and the dominant frequency peaks to estimate an optimal structure model near station KMMH16. The estimated velocity structure model indicates that the V_s values at shallower depths in the target area are substantially smaller compared to existing models. Also, the depth to the bedrock layer might be much deeper (about 600 m), in comparison with the existing model from logging data (234 m). The earthquake R/V spectral ratios at station KMMH16 also show the common peak at 0.4 Hz, suggesting that the similarity of deeper structures between the KiK-net station and our observation area in the severely damaged zone. Therefore, mainshock data recorded in the borehole at station KMMH16 could be directly used as input motions for seismic response analysis in the damaged zone.

Additional file

Additional file 1. Fig.S1: Observed accelerograms and Fourier amplitude spectra at KiK-net KMMH16 and Hi-net N.MSIH stations. **a** Comparisons of the observed three-component acceleration records, **b** Fourier amplitude spectra at KiK-net borehole station KMMH16 (black traces) and Hi-net station N.MSIH (red traces) for event EQ18. Note that the original velocity seismograms observed at N.MSIH have been differentiated after the removal of instrumental responses. **Fig. S2:** Four-day long power spectral density of the recorded seismic noise at site S6. Here the power is expressed as decibel (dB), which corresponds to $10\log_{10}(\text{m}^2/\text{s}^4/\text{Hz})$ of spectral acceleration.

Authors' contributions

TH, MY¹, JM, MY² and KH planned the survey, and TH, MY¹, MY², KH, JM, YF, HS, SF, EN, TO and AF participated in the observations. TH analyzed the observed data and MY¹ performed velocity structure inversions. TH, MY¹, MY², KH, JM and YF contributed to interpretations of the results. TH wrote the initial draft of the manuscript and MY¹ and JM edited it. All authors read and approved the final manuscript.

Author details

¹ International Institute of Seismology and Earthquake Engineering, Building Research Institute, 1 Tachihara, Tsukuba, Ibaraki 305-0802, Japan. ² Disaster Prevention Research Institute, Kyoto University, Gokasho, Uji, Kyoto 611-0011, Japan. ³ The New Japan Engineering Consultants Incorporated, 2-3-20 Honjo-Higashi, Kita-ku, Osaka 531-0074, Japan. ⁴ Graduate School of Science, Kyoto University, Gokasho, Uji, Kyoto 611-0011, Japan.

Acknowledgements

We appreciate two reviewers and Dr. Takuji Yamada for their helpful comments to improve the manuscript. We used the ground motion data from KiK-net and Hi-net Mashiki stations and referred a survey report of P-S logging at the site provided by NIED. We also used the unified earthquake catalogue and seismic intensity database published by JMA. Dr. Shin Koyama provided four sets of observation systems (SMAR-6A3P and LS-8800) for this survey. We would also like to show our gratitude to Dr. Hiroyuki Goto for showing us the modified S wave velocity model at station KMMH16 and Dr. Shigeki Senna for providing us a newly constructed 3D deep sedimentary structure model of Kumamoto plain, including Mashiki. We express our deepest gratitude to the local people in Mashiki for their understanding and cooperation with our observations.

Competing interests

The authors declare that they have no competing interests.

Availability of data and materials

Aftershock and microtremor data measured in this study (except site S4) are available to all interested researchers upon request, after the approval by all authors.

Ethics approval and consent to participate

Not applicable.

Funding

This work was partly supported by a research grant from the Kinki Kensetsu Association in FY2016.

Publisher's Note

Springer Nature remains neutral with regard to jurisdictional claims in published maps and institutional affiliations.

Received: 30 March 2018 Accepted: 28 June 2018

Published online: 11 July 2018

References

- Fukumoto S, Yamanaka H, Midorikawa S, Irie K (2004) Array measurements of microtremors and seismic motions for evaluating long-period ground motions—estimation of S-wave velocity structure and characteristics of surface-wave propagation in the Keiyo coastal area of the Kanto plain, Japan. *J Jpn Assoc Earthq Eng* 4(4):87–106. https://doi.org/10.5610/jaee.4.4_87 (in Japanese with English abstract)
- Gardner GHF, Gardner LW, Gregory AR (1974) Formation velocity and density—the diagnostic basics for stratigraphic traps. *Geophysics* 39(6):770–780. <https://doi.org/10.1190/1.1440465>
- Goto H, Hata Y, Yoshimi M, Yoshida N (2016) Non-linear site response at KiK-net Mashiki site. In: Proceedings of the 36th JSCE earthquake engineering symposium, Kanazawa Theatre, Kanazawa, 17–18 October 2016 (in Japanese with English abstract)
- Hayashi K, Martin A, Hatayama K, Kobayashi T (2013) Estimating deep S-wave velocity structure in the Los Angeles Basin using a passive surface-wave method. *Lead Edge* 32(6):620–626. <https://doi.org/10.1190/tle32060620>
- Kagawa T, Yoshida S, Ueno H (2017) Strong motion characteristics in the vicinity of surface fault rupture at suburbs of Mashiki Town due to the 2016 Kumamoto earthquake. *J Jpn Soc Civil Eng* 73(4):L_841–L_846. https://doi.org/10.2208/jscejsee.73.i_841 (in Japanese with English abstract)
- Kawase H, Matsushima S, Nagashima F, Baoyintu Nakano K (2017) The cause of heavy damage concentration in downtown Mashiki inferred from observed data and field survey of the 2016 Kumamoto earthquake. *Earth Planets Space* 69:3. <https://doi.org/10.1186/s40623-016-0591-1>
- Kitagawa Y, Hiraiishi H (2004) Overview of the 1995 Hyogo-ken Nanbu earthquake and proposals for earthquake mitigation measures. *J Jpn Assoc Earthq Eng* 4(3):1–29. https://doi.org/10.5610/jaee.4.3_1
- Mori T, Matsushita K, Kawasaki A (2017) Buildings and residential lands damage survey in Mashiki-machi, Kumamoto Prefecture on the 2016 Kumamoto earthquake. *Jpn Geotech J* 12(4):439–455. <https://doi.org/10.3208/jgs.12.439> (in Japanese with English abstract)
- Morikawa H, Sawada S, Akamatsu J (2004) A method to estimate phase velocities of Rayleigh waves using microseisms simultaneously observed at two sites. *Bull Seismol Soc Am* 94(3):961–976. <https://doi.org/10.1785/0120030020>
- Nagao T, Lohani TN, Fukushima Y, Ito Y, Hokugo A, Oshige J (2017) A study on the correlation between ground vibration characteristic and damage level of structures at Mashiki Town by the 2016 Kumamoto earthquake. *J Jpn Soc Civil Eng* 73(4):L_294–L_309. https://doi.org/10.2208/jscejsee.73.i_294 (in Japanese with English abstract)
- Nakagawa H, Kashiwa H, Arai H (2017) Dynamic deformation properties and ground motion amplification characteristics in Mashiki Town. Paper presented at the 13th annual meeting of JAE, the University of Tokyo, Tokyo, 13–14 November 2017 (in Japanese)
- National Institute for Land and Infrastructure Management and Building Research Institute (2016) Quick report of the field survey on the building damage by the 2016 Kumamoto earthquake. Technical note of NILIM 929/building research data 173, Tsukuba (in Japanese with English abstract)
- Ogawa N, Suzuki H, Senna S, Jin K, Wakai A, Matsuyama H, Sakurai K, Yatagai A, Komazawa M (2017) 3D subsurface structural model using microtremor array measurements for strong motion simulation around Kumamoto plain. In: Abstracts of the 136th SEGJ conference, Waseda University, Tokyo, 5–7 June 2017 (in Japanese)
- Okada S, Takai N (1999) Classifications of structural types and damage patterns of buildings for earthquake field investigation. *J Struct Constr Eng Trans AIJ* 64(524):65–72. https://doi.org/10.3130/aijs.64.65_5 (in Japanese with English abstract)
- Saito M (1988) DISPER80: a subroutine package for the calculation of seismic normal mode solutions. In: Doorn-bos DJ (ed) *Seismological Algorithms*. Academic Press, New York, pp 293–319
- Sakai Y, Nojiri S, Kumamoto T, Tanaka Y (2008) Damage investigation of surroundings of the seismic stations in the 2007 Noto-hanto earthquake and correspondence of damage to buildings with strong ground motions. *J Jpn Assoc Earthq Eng* 8(3):79–106. https://doi.org/10.5610/jaee.8.3_79 (in Japanese with English abstract)
- Senna S, Wakai A, Jin K, Cho I, Matsuyama H, Yatagai A, Fujiwara H (2017a) Modeling of the subsurface structure from the seismic bedrock to the ground surface for a broadband strong motion evaluation in Kumamoto plain. In: Abstracts of the 136th SEGJ conference, Waseda University, Tokyo, 5–7 June 2017 (in Japanese)
- Senna S, Wakai A, Jin K, Matsuyama H, Fujiwara H (2017b) Modeling of the subsurface structure from the seismic bedrock to the ground surface for a broadband strong motion evaluation in Kumamoto plain. In: Abstracts of the 2017 AGU fall meeting, Ernest N. Morial Convention Center, New Orleans, 11–15 December 2017
- Shingaki Y, Yoshimi Y, Goto H, Kurita T, Sato K, Hosoya Y, Arai Y, Morita S (2017) Physical and dynamic properties of the volcanic ash soil in the heavily damaged site of the 2016 Kumamoto earthquake, Mashiki Town. *J Jpn Soc Civil Eng* 73(3):552–559. <https://doi.org/10.2208/jscejsee.73.552> (in Japanese with English abstract)
- Shirahama Y, Yoshimi M, Awata Y, Maruyama T, Azuma T, Miyashita Y, Mori H, Imanishi K, Takeda N, Ochi T, Otsubo M, Asahina D, Miyakawa A (2016) Characteristics of the surface ruptures associated with the 2016

- Kumamoto earthquake sequence, central Kyushu, Japan. *Earth Planets Space* 68:191. <https://doi.org/10.1186/s40623-016-0559-1>
- Sugino M, Ohmura S, Tokuoka S, Hayashi Y (2016a) Maximum response evaluation of traditional wooden houses based on microtremor measurements. *J Struct Constr Eng Trans AIJ* 81(729):1869–1879. <https://doi.org/10.3130/aajs.81.1869> **(in Japanese with English abstract)**
- Sugino M, Yamanuro R, Kobayashi S, Murase S, Ohmura S, Hayashi Y (2016b) Analyses of building damages in Mashiki Town in the 2016 Kumamoto earthquake. *J Jpn Assoc Earthq Eng* 16(10):10_69–10_83. https://doi.org/10.5610/jaee.16.10_69 **(in Japanese with English abstract)**
- Sugito N, Goto H, Kumahara Y, Tsutsumi H, Nakata T, Kagohara K, Matsuta N, Yoshida H (2016) Surface fault ruptures associated with the 14 April foreshock (Mj 6.5) of the 2016 Kumamoto earthquake sequence, southwest Japan. *Earth Planets Space* 68:170. <https://doi.org/10.1186/s40623-016-0547-5>
- Suzuki Y, Watanabe M, Nakata T (2016) Problems and recommendations for active fault and disaster mitigation learned from the 2016 Kumamoto earthquake. *Kagaku* 86(8):839–847 **(in Japanese)**
- Toda S, Kaneda H, Okada S, Ishimura D, Mildon ZK (2016) Slip-partitioned surface ruptures for the Mw 7.0 16 April 2016 Kumamoto, Japan, earthquake. *Earth Planets Space* 68:188. <https://doi.org/10.1186/s40623-016-0560-8>
- Tomozawa Y, Motoki K, Kato K, Hikita T, Ishiki K (2017) Investigation of tombstones fall-down rates and damages of wooden houses due to the 2016 Kumamoto earthquake—comparative examination of near-fault region and Mashiki-machi Miyazono. *J Jpn Assoc Earthq Eng* 17(4):4_62–4_80. https://doi.org/10.5610/jaee.17.4_62 **(in Japanese with English abstract)**
- Yamada M (2017) Damage islands in Mashiki Town from the 2016 Kumamoto earthquakes. *J Jpn Assoc Earthq Eng* 17(5):5_38–5_47. https://doi.org/10.5610/jaee.17.5_38 **(in Japanese with English abstract)**
- Yamada M, Mori J, Yamada M, Hada K, Fujino Y, Hayashida T (2017a) Unconventional damage patterns in Mashiki town during the 2016 Kumamoto earthquakes. In: Abstracts of the 2017 AGU fall meeting, Ernest N. Morial Convention Center, New Orleans, 11–15 December 2017
- Yamada M, Omura J, Goto H (2017b) Wooden building damage analysis in Mashiki Town for the 2016 Kumamoto earthquakes on April 14 and 16. *Earthq Spectra* 33(4):1555–1572. <https://doi.org/10.1193/090816EQS144M>
- Yamada M, Yamada M, Mori J, Sakaue H, Hayashida T, Hada K, Fujino Y, Fukatsu S, Nishihara E, Ouchi T, Fujii A (2017c) Investigation of building damage in Mashiki-town for the 2016 Kumamoto earthquake—effect of local soil conditions. *J Jpn Soc Civil Eng* 73(4):l_216–l_224. https://doi.org/10.2208/jscejsee.73.i_216 **(in Japanese with English abstract)**
- Yamanaka H, Ishida H (1996) Application of genetic algorithms to an inversion of surface-wave dispersion data. *Bull Seismol Soc Am* 86(2):436–444
- Yamanaka H, Chimoto K, Miyake H, Tsuno S, Yamada N (2016) Observation of earthquake ground motion due to aftershocks of the 2016 Kumamoto earthquake in damaged areas. *Earth Planets Space* 68:197. <https://doi.org/10.1186/s40623-016-0574-2>
- Yoshimi M, Goto H, Haya Y, Yoshida N (2017) Nonlinear site response at the worst-hit area of the 2016 Kumamoto earthquakes in the Mashiki Town, Kumamoto, Japan. In: Abstracts of the 2017 disaster prevention research institute annual meeting, Kyoto University, Uji, 21–22 February 2017 **(in Japanese with English abstract)**

Submit your manuscript to a SpringerOpen[®] journal and benefit from:

- Convenient online submission
- Rigorous peer review
- Open access: articles freely available online
- High visibility within the field
- Retaining the copyright to your article

Submit your next manuscript at ► springeropen.com
